CrossMark

JWST's PEARLS: A JWST/NIRCam View of ALMA Sources

Cheng Cheng[1,2], Jia-Sheng Huang[1,3], Ian Smail[4], Haojing Yan[5], Seth H. Cohen[6], Rolf A. Jansen[6],
Rogier A. Windhorst[6], Zhiyuan Ma[7], Anton Koekemoer[8], Christopher N. A. Willmer[9], S. P. Willner[3],
Jose M. Diego[10], Brenda Frye[11], Christopher J. Conselice[12], Leonardo Ferreira[13], Andreea Petric[8], Min Yun[7],
Hansung B. Gim[14], Maria del Carmen Polletta[15], Kenneth J. Duncan[16], Benne W. Holwerda[17], Huub J. A. Röttgering[18],
Rachel Honor[6], Nimish P. Hathi[8], Patrick S. Kamieneski[7], Nathan J. Adams[12], Dan Coe[8,19,20],
Tom Broadhurst[21,22,23], Jake Summers[6], Scott Tompkins[6], Simon P. Driver[24], Norman A. Grogin[8],
Madeline A. Marshall[25,26], Nor Pirzkal[8], Aaron Robotham[24], and Russell E. Ryan, Jr.[8]
[1] Chinese Academy of Sciences South America Center for Astronomy, National Astronomical Observatories, CAS, Beijing 100101, People's Republic of China
yanha@missouri.edu
[2] CAS Key Laboratory of Optical Astronomy, National Astronomical Observatories, Chinese Academy of Sciences, Beijing 100101, People's Republic of China
[3] Center for Astrophysics | Harvard & Smithsonian, 60 Garden St., Cambridge, MA 02138, USA
[4] Centre for Extragalactic Astronomy, Department of Physics, Durham University, South Road, Durham DH1 3LE, UK
[5] Department of Physics and Astronomy, University of Missouri, Columbia, MO 65211, USA
[6] School of Earth and Space Exploration, Arizona State University, Tempe, AZ 85287-1404, USA
[7] Department of Astronomy, University of Massachusetts, Amherst, MA 01003, USA
[8] Space Telescope Science Institute, 3700 San Martin Drive, Baltimore, MD 21218, USA
[9] Steward Observatory, University of Arizona, 933 N Cherry Ave, Tucson, AZ 85721-0009, USA
[10] Instituto de Física de Cantabria (CSIC-UC), Avenida. Los Castros s/n. E-39005 Santander, Spain
[11] University of Arizona, Department of Astronomy/Steward Observatory, 933 N Cherry Ave., Tucson, AZ 85721, USA
[12] Jodrell Bank Centre for Astrophysics, Alan Turing Building, University of Manchester, Oxford Road, Manchester M13 9PL, UK
[13] University of Nottingham, School of Physics & Astronomy, Nottingham NG7 2RD, UK
[14] Department of Physics, Montana State University, P.O. Box 173840, Bozeman, MT 59717, USA
[15] INAF, Istituto di Astrofisica Spaziale e Fisica cosmica (IASF) Milano, Via A. Corti 12, I-20133 Milan, Italy
[16] Institute for Astronomy, Royal Observatory, Blackford Hill, Edinburgh EH9 3HJ, UK
[17] Department of Physics and Astronomy, University of Louisville, Louisville, KY 40292, USA
[18] Leiden Observatory, PO Box 9513, 2300 RA Leiden, The Netherlands
[19] Association of Universities for Research in Astronomy (AURA) for the European Space Agency (ESA), STScI, Baltimore, MD 21218, USA
[20] Center for Astrophysical Sciences, Department of Physics and Astronomy, The Johns Hopkins University, 3400 N Charles St. Baltimore, MD 21218, USA
[21] Department of Theoretical Physics, University of the Basque Country UPV-EHU, E-48040 Bilbao, Spain
[22] Donostia International Physics Center (DIPC), E-20018 Donostia, The Basque Country, Spain
[23] IKERBASQUE, Basque Foundation for Science, Alameda Urquijo, 36-5 E-48008 Bilbao, Spain
[24] International Centre for Radio Astronomy Research (ICRAR) and the International Space Centre (ISC), The University of Western Australia, M468, 35 Stirling
Highway, Crawley, WA 6009, Australia
[25] National Research Council of Canada, Herzberg Astronomy & Astrophysics Research Centre, 5071 West Saanich Road, Victoria, BC V9E 2E7, Canada
[26] ARC Centre of Excellence for All Sky Astrophysics in 3 Dimensions (ASTRO 3D), Australia

Abstract

We report the results of James Webb Space Telescope/NIRCam observations of 19 (sub)millimeter sources detected by the Atacama Large Millimeter Array (ALMA). The accurate ALMA positions allowed unambiguous identifications of their NIRCam counterparts. Taking gravitational lensing into account, these represent 16 distinct galaxies in three fields and constitute the largest sample of its kind to date. The counterparts' spectral energy distributions cover from rest-frame ultraviolet to near-IR and provide photometric redshifts ($1 < z < 4.5$) and stellar masses ($M_* > 10^{10.5} M_\odot$), which are similar to submillimeter galaxies (SMGs) studied previously. However, our sample is fainter in (sub)millimeter than the classic SMG samples are, and our sources exhibit a wider range of properties. They have dust-embedded star formation rates as low as $10 M_\odot \, \mathrm{yr}^{-1}$, and the sources populate both the star-forming main sequence and the quiescent categories. The deep NIRCam data allow us to study the rest-frame near-IR morphologies. Excluding two multiply imaged systems and one quasar, the majority of the remaining sources are disk-like and show either little or no disturbance. This suggests that secular growth is a potential route for the assembly of high-mass disk galaxies. While a few objects have large disks, the majority have small disks (median half-mass radius of 1.6 kpc). At this time, it is unclear whether this is due to the prevalence of small disks at these redshifts or some unknown selection effects of deep ALMA observations. A larger sample of ALMA sources with NIRCam observations will be able to address this question.

Unified Astronomy Thesaurus concepts: Millimeter astronomy (1061); Submillimeter astronomy (1647); Galaxy formation (595); Infrared galaxies (790); James Webb Space Telescope (2291)

1. Introduction

The submillimeter/millimeter window offers a view of the high-redshift galaxy population complementary to that seen in visible light (e.g., Smail et al. 1997; Casey et al. 2014). Sources detected in this window are commonly referred to as

submillimeter galaxies (SMGs). Follow-up studies have shown that SMGs are mainly high-redshift ($z \sim 2$–3), dusty, and star-forming galaxies, and most of the brightest SMGs are gravitationally magnified by foreground massive galaxies or clusters (Blain 1996; Blain et al. 2002; Perrotta et al. 2002; Negrello et al. 2010, 2017). Over the years, finding SMGs has become one of the most efficient methods to select dusty star-forming galaxies (DSFGs) at high redshifts.

Despite many successes, SMG studies have been limited by the poor angular resolution of single-dish telescopes through which SMGs have been selected. The low resolution makes the source positions uncertain. More recently, interferometry arrays such as the Atacama Large Millimeter/submillimeter Array (ALMA) have been used to locate SMGs and allow unambiguous identification of their counterparts (e.g., Hodge et al. 2013). This has allowed studies of SMGs using exquisite Hubble Space Telescope (HST) images (e.g., Chen et al. 2015; Hodge et al. 2016; Dunlop et al. 2017; Hodge et al. 2019; Stach et al. 2019; Cheng et al. 2020; Cardona-Torres et al. 2022). Due to the high redshifts where SMGs reside, however, HST only sees them in the rest-frame UV-to-visible wavelengths, where SMGs have severe dust extinction. This makes it difficult to obtain a comprehensive picture of their underlying stellar populations. Spitzer/IRAC images of SMGs probe them in the rest-frame near-IR but have only $\sim 2''$ angular resolution, which is insufficient to study the host morphologies. The low resolution also often leads to blended IRAC images, which can make it difficult to derive accurate spectral energy distributions (SEDs).

JWST promises to overcome prior limitations in infrared studies of SMGs (Cheng et al. 2022; Zavala et al. 2022; Chen et al. 2022). The NIRCam instrument offers ~ 0.7–5 μm images with angular resolution comparable to that of HST. Provided that accurate positions are known (e.g., from ALMA), NIRCam images can reveal the host stellar distributions and allow accurate SED measurements to enable detailed diagnostics of the underlying stellar populations.

This paper presents the JWST/NIRCam view of 19 submillimeter/millimeter sources (16 distinct galaxies) from the ALMA archival data in three well-studied fields, which form the largest sample of its kind to date. The JWST/NIRCam data come from the Prime Extragalactic Areas for Reionization and Lensing Science program (PEARLS; Windhorst et al. 2023) and the archival data from the Public Release IMaging for Extragalactic Research (PRIMER; Dunlop et al. 2021, PI: James Dunlop,). Accurate positions are available from the ALMA 92, 260, or 340 GHz maps, making counterpart identification possible. Section 2 of this paper describes the data, and Section 3 presents the results. A summary is in Section 4. Throughout this paper, magnitudes are in the AB system, and we adopt a flat ΛCDM cosmology with $H_0 = 70$ km s^{-1} Mpc^{-1}, $\Omega_M = 0.3$, and $\Omega_\Lambda = 0.7$.

2. Data and Sample

2.1. Field Description

Our sample is collected from three fields that have both ALMA archival data and new JWST/NIRCam data. ACT-CL J0102−4915 (nicknamed "El Gordo") is a high-mass ($M_{\rm tot} \sim 10^{15}\, M_\odot$), colliding galaxy cluster at $z = 0.87$ (Menanteau et al. 2010, 2012; Marriage et al. 2011; Jee et al. 2014; Lindner et al. 2014). It was selected as a PEARLS field because it is a

powerful cosmic lens. Its lensing properties have been modeled based on lensed background objects detected by HST (Zitrin et al. 2013; Diego et al. 2020) and more recently by the PEARLS team (Diego et al. 2022; B. Frye et al. 2022, in preparation) using JWST data.

TN J1338 + 1942 (hereafter "TNJ1338") is a radio galaxy at $z = 4.11$ (De Breuck et al. 1999) and is the dominant member of a protocluster (Venemans et al. 2002; Miley et al. 2004). It was selected as a PEARLS field primarily for the study of galaxy properties in a protocluster environment.

The UKIDSS Ultra-Deep Survey field (hereafter "UDS"—Stach et al. 2018) is one of the most-studied extragalactic survey fields and is where PRIMER will carry out the majority of its JWST observations.

2.2. ALMA Archive Data and Sample Construction

The El Gordo field has been observed by the ALMA programs 2013.1.01358.S (PI: A. Baker) and 2018.1.00035.L (PI: K. Kohno) in Band 6 (270 GHz = 1.1 mm) and 2013.1.01051.S (PI: P. Aguirre) in Band 7 (340 GHz = 870 μm). The ALMA data in the TNJ1338 field were obtained by program 2015.1.00530.S (PI: C. De Breuck) in Band 3 (92 GHz = 3.3 mm). The UDS has a large number of ALMA programs. In the current PRIMER UDS field, the ALMA Band 6 and/or Band 7 data were collected by Astroquery in each PRIMER observation region. These archival data were reduced by the Chinese South American Center ALMA data processing program (C. Cheng et al. 2023, in preparation). Briefly, the data were calibrated by the default ALMA data reduction script SCRIPTFORPI.PY. The task TCLEAN in CASA 6.2.1 (McMullin et al. 2007) was used to clean the data to build the continuum images. For this set of data, the clean parameters were set to WEIGHTING = "BRIGGS" and ROBUST = 2.0, and we cleaned the images to 3σ.

The final 1.1 mm map in El Gordo has beam size $1''28 \times 0''93$ at PA = $88°$ and reaches ~ 0.065 mJy beam^{-1} (rms). This map has an area of ~ 4 arcmin^2 overlapped with the NIRCam coverage (see below) and was used for the source detection in this field. The final 870 μm map, which covers only a portion of the 1.1 mm map, reaches 0.25 mJy beam^{-1} with beam size $0''33 \times 0''40$ at PA = $-35°$.

In TNJ1338, the final 3.3 mm map has beam size of $2''11 \times 1''74$, PA = $-82°$ and reaches ~ 0.009 mJy beam^{-1} rms. It covers ~ 2 arcmin^2, centered around the radio galaxy.

In the UDS field, the final images have beam sizes of about $0''7$ at 1.1 mm and $0''4$ at 870 μm. The total coverage is ~ 1 arcmin^2. Both images reach rms ~ 0.05 mJy. The source detections were done in both bands, and the results were merged.

Source extraction was done by running SExtractor (Bertin & Arnouts 1996) in dual-image mode. The detection was done on the ALMA maps not corrected for the primary-beam attenuation, as these have a uniform noise distribution. The photometry was done on the primary-beam-corrected images exported from CASA. The detection map was convolved using a Gaussian kernel, and we set DETECT_THRESH = 4. FLUX_AUTO was adopted for the flux density measurements. To account for the calibration uncertainty, we added in quadrature 10% of the flux density (Fomalont et al. 2014) to the reported FLUXERR_AUTO to obtain the final uncertainty estimate. All these detections have signal-to-noise ratios (S/Ns) higher than 3, and all but two have S/N > 5 (see Table 1).

Table 1
ALMA Source Catalog

Name	R.A. J2000	Decl. J2000	$S_{870\mu m}$ (mJy)	$S_{1.1mm}$ (mJy)	$S_{3.3mm}$ (mJy)	Redshift	$\log(M_*)$ $\log(M_\odot)$	$\log(SFR)$ $\log(M_\odot\,yr^{-1})$	R_e(NIR) (kpc)	μ
EG-ALMA 2a	01:02:49.2	−49:15:08.7	⋯	0.32 ± 0.03	⋯	3.58 ± 0.38[a]	⋯	⋯	⋯	4.6
EG-ALMA 2b	01:02:49.4	−49:15:05.3	1.62 ± 0.12	0.65 ± 0.07	⋯	3.58 ± 0.38[a]	⋯	⋯	⋯	5.5
EG-ALMA 3	01:02:49.3	−49:14:38.1	⋯	0.75 ± 0.08	⋯	2.34 ± 0.51	10.94 ± 0.11	1.94 ± 0.49	5.35 ± 0.27	2.1
EG-ALMA 5	01:02:50.5	−49:15:41.7	⋯	0.25 ± 0.03	⋯	2.49 ± 0.30	11.13 ± 0.14	1.09 ± 0.44	1.53 ± 0.30	1.8
EG-ALMA 6a	01:02:51.1	−49:15:38.8	⋯	0.90 ± 0.09	⋯	4.324[b]	⋯	⋯	⋯	3.9
EG-ALMA 6b	01:02:54.9	−49:15:14.7	1.37 ± 0.15	1.24 ± 0.12	⋯	4.324[b]	⋯	⋯	⋯	3.1
EG-ALMA 6 c	01:02:55.7	−49:15:09.0	1.89 ± 0.19	0.99 ± 0.10	⋯	4.324[b]	10.14 ± 0.10	1.97 ± 0.14	1.80 ± 0.10	10.0
EG-ALMA 11	01:02:57.7	−49:15:20.0	⋯	0.11 ± 0.01	⋯	1.67 ± 0.21	10.96 ± 0.11	1.08 ± 0.46	2.27 ± 0.27	2.3
EG-ALMA 12	01:02:58.1	−49:14:56.2	⋯	0.63 ± 0.07	⋯	2.49 ± 0.18	10.91 ± 0.15	0.98 ± 0.58	1.63 ± 0.34	1.4
EG-ALMA 13	01:03:00.2	−49:16:03.4	⋯	0.17 ± 0.02	⋯	1.80 ± 1.08	10.48 ± 0.12	1.32 ± 0.62	1.08 ± 0.21	3.2
UDS-ALMA 1	02:17:19.6	−05:09:41.4	4.91 ± 1.54	⋯	⋯	2.10 ± 0.13	11.15 ± 0.08	2.30 ± 0.38	1.18 ± 0.42	1
UDS-ALMA 2	02:17:21.0	−05:08:37.2	⋯	0.93 ± 0.16	⋯	2.08 ± 0.06[c]	⋯	⋯	< 0.80	1
UDS-ALMA 3	02:17:22.3	−05:10:38.6	⋯	1.02 ± 0.13	⋯	1.089[d]	11.55 ± 0.14	1.75 ± 0.64	2.54 ± 0.39	1
UDS-ALMA 4	02:17:26.1	−05:10:58.3	3.04 ± 0.38	0.86 ± 0.09	⋯	1.74 ± 0.38	11.18 ± 0.19	2.42 ± 0.37	4.64 ± 0.42	1
UDS-ALMA 5	02:17:27.2	−05:11:57.8	6.31 ± 0.65	2.43 ± 0.57	⋯	2.154[d]	11.32 ± 0.08	2.33 ± 0.22	3.78 ± 0.41	1
UDS-ALMA 6	02:17:43.9	−05:07:51.3	2.19 ± 0.26	⋯	⋯	2.51 ± 0.28	11.31 ± 0.07	2.28 ± 0.36	1.44 ± 0.40	1
TN-ALMA 1	13:38:24.9	−19:42:15.8	⋯	⋯	0.057 ± 0.006	3.17 ± 1.03	10.77 ± 0.40	2.36 ± 0.33	1.12 ± 0.42	1
TN-ALMA 2	13:38:25.7	−19:42:34.6	⋯	⋯	0.046 ± 0.005	3.39 ± 0.26	10.58 ± 0.09	2.17 ± 0.31	1.20 ± 0.39	1
TN-ALMA 6	13:38:26.9	−19:42:30.9	⋯	⋯	0.031 ± 0.003	1.47 ± 0.46	11.35 ± 0.10	2.05 ± 0.46	2.80 ± 0.41	1

Notes. The flux densities, masses, SFRs, and sizes for the El Gordo sources have been corrected for the gravitational lensing magnification μ. For most objects, their z_{phot} from MAGPHYS-PHOTOZ are listed in the "Redshift" column. The exceptions are (1) the objects that have z_{spec}, for which their z_{spec} are listed; and (2) the point-like source UDS-ALMA 2, for which we adopt z_{phot} from EAZY as it was derived using AGN templates and is more plausible. R_e is for the disk component (i.e., with a point-source core subtracted for UDS-ALMA 1/3/4/5). Because R_e is measured in the rest-frame near-IR, it is equivalent to the half-mass radius.
[a] Lensed double images of a single source (see Diego et al. 2022).
[b] Lensed triple images of a single source. Its z_{spec} is based on CO $J = 4$–3 emission line (see Appendix B) and has uncertainty 0.001.
[c] z_{phot} derived by EAZY using AGN templates.
[d] z_{spec} from Lang et al. (2019), Bourne et al. (2019). The typical z_{spec} uncertainty is 0.001.

2.3. JWST NIRCam Data

The PEARLS NIRCam data in the TNJ1338 field and the El Gordo field were taken on 2022 July 1 and 29, respectively, and these observations are described by Windhorst et al. (2023). Briefly, the observations of El Gordo were done in F090W, F115W, F150W, F200W, F277W, F356W, F410M, and F444W, and the total integration times were 2491, 2491, 1890, 2104, 2104, 1890, 2491, and 2491 s, respectively. The observations in TNJ1338 were done in F150W, F182M, F210M, F300M, F335M, and F360M with a uniform total integration time of 1031 s in each band. In both fields, the areas where the ALMA data reside are covered by one NIRCam module (module B).

As of this writing, only a small fraction of the PRIMER observations in UDS were executed, all on 2022 July 29. The NIRCam data were taken in three pointings as the parallels to the primary MIRI observations. One pointing is isolated, while the other two overlap and fill the wide gaps between the two NIRCam modules. The passbands used were the same as for El Gordo, but integration times were 837 s in each band.

All data were reduced using the JWST data reduction pipeline version 1.6.1dev3+gad99335d in the context of jwst_0944.pmap, starting from the Stage 1 "uncal" products. A few changes and augmentations were made to the pipeline to improve the reduction quality (Yan et al. 2022). In the El Gordo field, the final stacked images were created at a pixel scale 0.″06 and were aligned to the existing HST images of the same scale produced by the Reionization Lensing Cluster Survey (Coe et al. 2019). The final stacks in the TNJ1338 field were also aligned to the existing HST images, which are available from the High Level Science Products provided by the Mikulski Archive for Space Telescopes. These HST images have pixel scale of 0.″04, and the NIRCam images were created at the same scale. In the UDS field, the final stacks were created at 0.″06 pixel^{-1} and were aligned to the existing HST images of the same scale from the Cosmic Assembly Near-infrared Deep Extragalactic Legacy Survey (CANDELS; Grogin et al. 2011; Koekemoer et al. 2011).

In total, we identified 10, 4, and 6 NIRCam counterparts of our ALMA sources in the El Gordo, TNJ1338, and UDS fields, respectively. One of the TNJ1338 sources is the central radio galaxy, which is studied by Duncan et al. (2022) and not discussed further here. Table 1 lists the remaining 19 sources. Figure 1 shows the HST/Advanced Camera for Surveys (ACS) and NIRCam stamp images for each. The sources in the El Gordo field are affected by gravitational lensing to various degrees. In particular, EG-ALMA 6a/6b/6c are the triple images of a single galaxy that is believed to be associated with the $z = 4.32$ galaxy group (Caputi et al. 2021). EG-ALMA 2a/2b are two images of another single galaxy lensed by two cluster-member galaxies as well as the cluster as a whole. Therefore, the 10 sources in this field correspond to seven unique galaxies; and so our final sample consists of 16 galaxies.

3. Analysis and Results

3.1. SED Construction and Fitting

For the targets in the El Gordo field, we did not use the HST data because the JWST NIRCam data alone sufficiently sample the rest-frame visible-to-near-IR range. In the UDS field, UDS-ALMA 4 has no NIRCam data in the short wavelength bands because it falls in the gap in between the modules. Therefore,

we used the HST data in F606W, F814W, F125W, and F160W. For homogeneity, these HST images were also used for the other UDS targets. In TNJ1338, the bluest NIRCam band is F150W, and therefore we added HST F775W and F850LP data to extend the wavelength sampling to visible wavelengths.

We used SExtractor in dual-image mode for photometry. For the sources in El Gordo and UDS, the detection band was set to F444W; in TNJ1338, it was set to F360M. In most cases, we adopted MAG_ISO to optimize the S/N for the best color measurement. The exceptions were the two multiply imaged systems EG-ALMA 2a/2b and EG-ALMA 6a/6b/6c. The former is blended with two cluster-member galaxies, which contribute the major part of the lensing effect that creates this system. The latter has a close neighbor that might be associated with the source but is not the counterpart. In both cases, their MAG_ISO apertures are severely contaminated by the light from these neighbors. To minimize the contamination, we had to derive colors using a circular aperture of 0.″6 in diameter centered on the position of the brightest pixel in the F444W image.

Figure 2 shows the full SEDs, combining rest-frame visible-to-near-IR photometry with the ALMA photometry. We used MAGPHYS+PHOTOZ (da Cunha et al. 2008; Battisti et al. 2019) to fit these SEDs to obtain physical properties of the hosts, most importantly the photometric redshift (z_{phot}), the star formation rate (SFR), and the stellar mass (M_*). The best-fit results are shown in Figure 2, and the derived values are presented in Table 1. The SFR and M_* values for the El Gordo sources have been corrected for the magnification factors (μ) at the corresponding redshifts. Two sources, UDS-ALMA 3 and 5, have spectroscopic redshifts (z_{spec}), which are quoted in Table 1; their M_* and SFR listed in the table were derived at their z_{spec}, while Figure 2 still shows their SED-fitting results when treating redshift as a free parameter.

MAGPHYS+PHOTOZ is designed to fit panchromatic SEDs based on the "energy-balance" premise, which argues that the UV-to-near-IR energy absorbed by dust in a system should roughly equal the far-IR-to-millimeter light reemitted by dust. This approach provides a good constraint on the amount of dust extinction, and propagates the uncertainty of z_{phot} to the uncertainties in other derived parameters. However, the energy-balance premise might not hold if the dust component is not well mixed with stars in the host galaxy. In addition, we have only one or two ALMA bands constraining the dust emission. To check the robustness of the z_{phot} derived by MAGPHYS +PHOTOZ, we also fitted the visible-to-near-IR SEDs using EAZY (Brammer et al. 2008) with EAZY_V1.1_LINES.SPECTRA. PARAM templates to derive z_{phot} independently. The best-fit results are summarized in Figure 3. For most sources, these two sets of z_{phot} are consistent with each other (see Appendix A), which gives us confidence in the results obtained by MAGPHYS +PHOTOZ.

EG-ALMA 2a/2b and EG-ALMA 6a/6b/6c are two multiply imaged systems. (The latter has z_{spec} from the ALMA spectroscopy; see Appendix B.) It is difficult to obtain reliable photometry for them because the images are highly distorted. This is reflected in the disagreement in z_{phot} values for the individual images and for the same image as measured by the two different methods. We have therefore excluded these objects from the later discussion. We also exclude UDS-ALMA 2, which is likely a quasar, for most purposes.
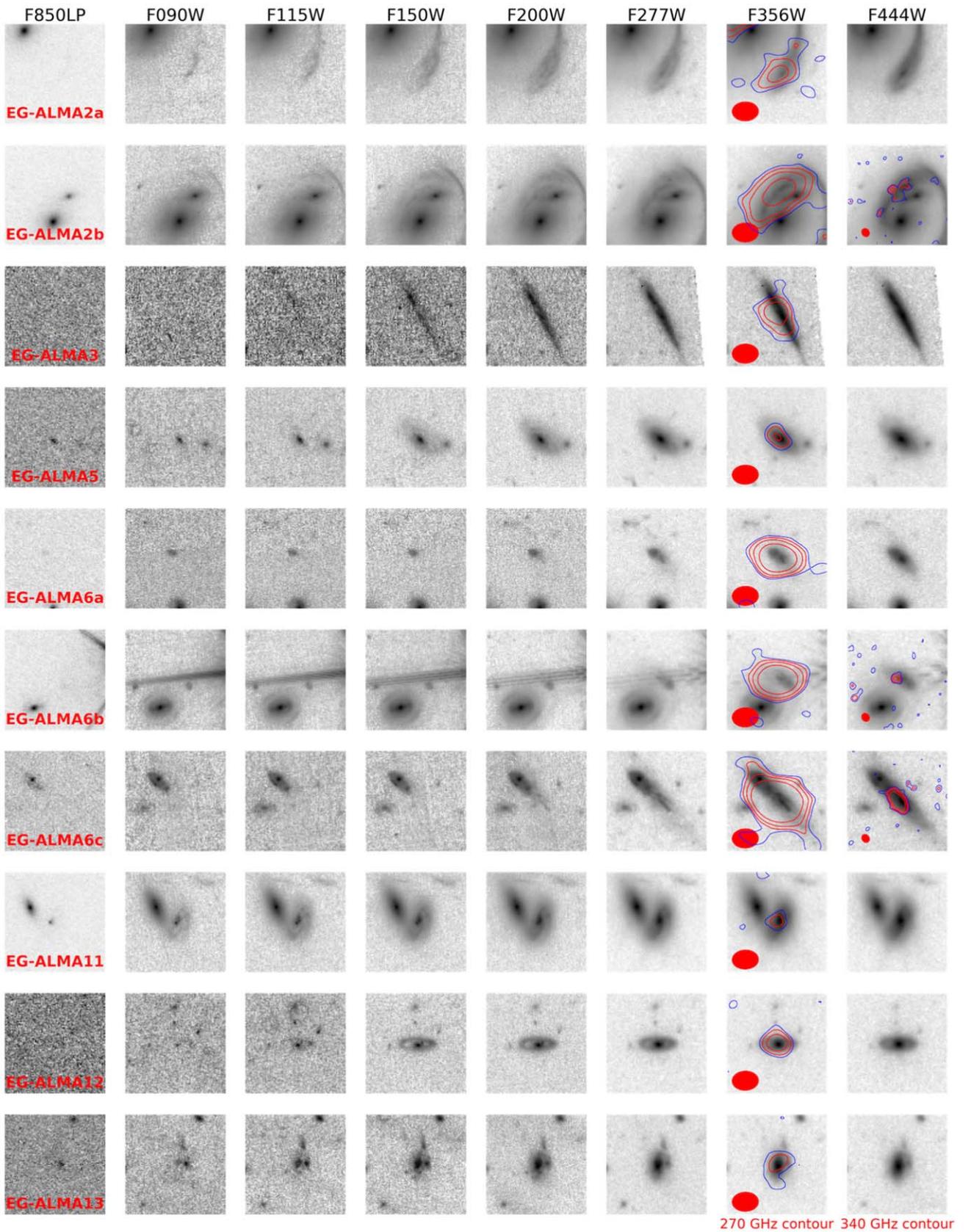
Figure 1. (a) Images of the ALMA sources in El Gordo, one source in each row. Each stamp is $5'' \times 5''$ in size. Both the archival HST ACS images (F850LP or F814W) and the new JWST NIRCam images (F090W to F444W) are shown with bandpass filters noted at top. The ALMA Band 6 (1.1 mm) contours (2σ in blue; 3, 5, and 10σ in red) are superposed on the F356W images, and the Band 7 (870 μm) contours when available are superposed on the F444W images (using the same contour color-coding as for Band 6). The ALMA beams are shown as the red-filled ellipses. (b) Images of the ALMA sources in UDS. The images are $5'' \times 5''$ in size. (c) Images of the ALMA sources in TNJ1338. The images are $10'' \times 10''$ in size.
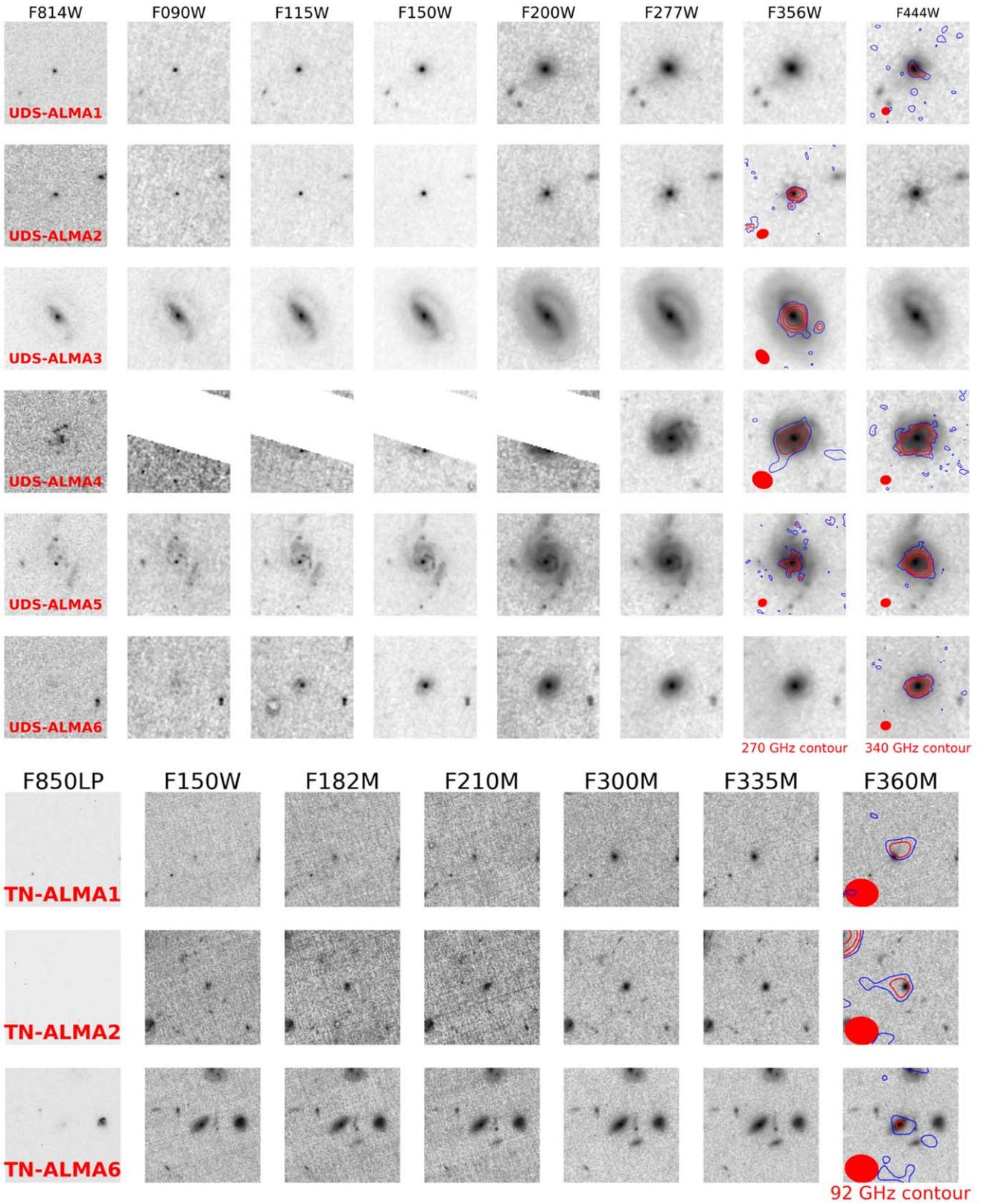
Figure 1. (Continued.)

3.2. Host Galaxy Star Formation: From Star-forming to Quiescent

Figure 4 (left) compares these ALMA source hosts to the "star formation main sequence" from Speagle et al. (2014). Excluding EG-ALMA 2a/2b, EG-ALMA 6a/6b/6 c, and UDS-ALMA 2, all other sources have $M_* \geqslant 10^{10.5} \ M_\odot$, in line with the general SMG population. However, three objects have SFR $\leqslant 16 \ M_\odot \, \mathrm{yr}^{-1}$, which puts them well below the main sequence. This is more
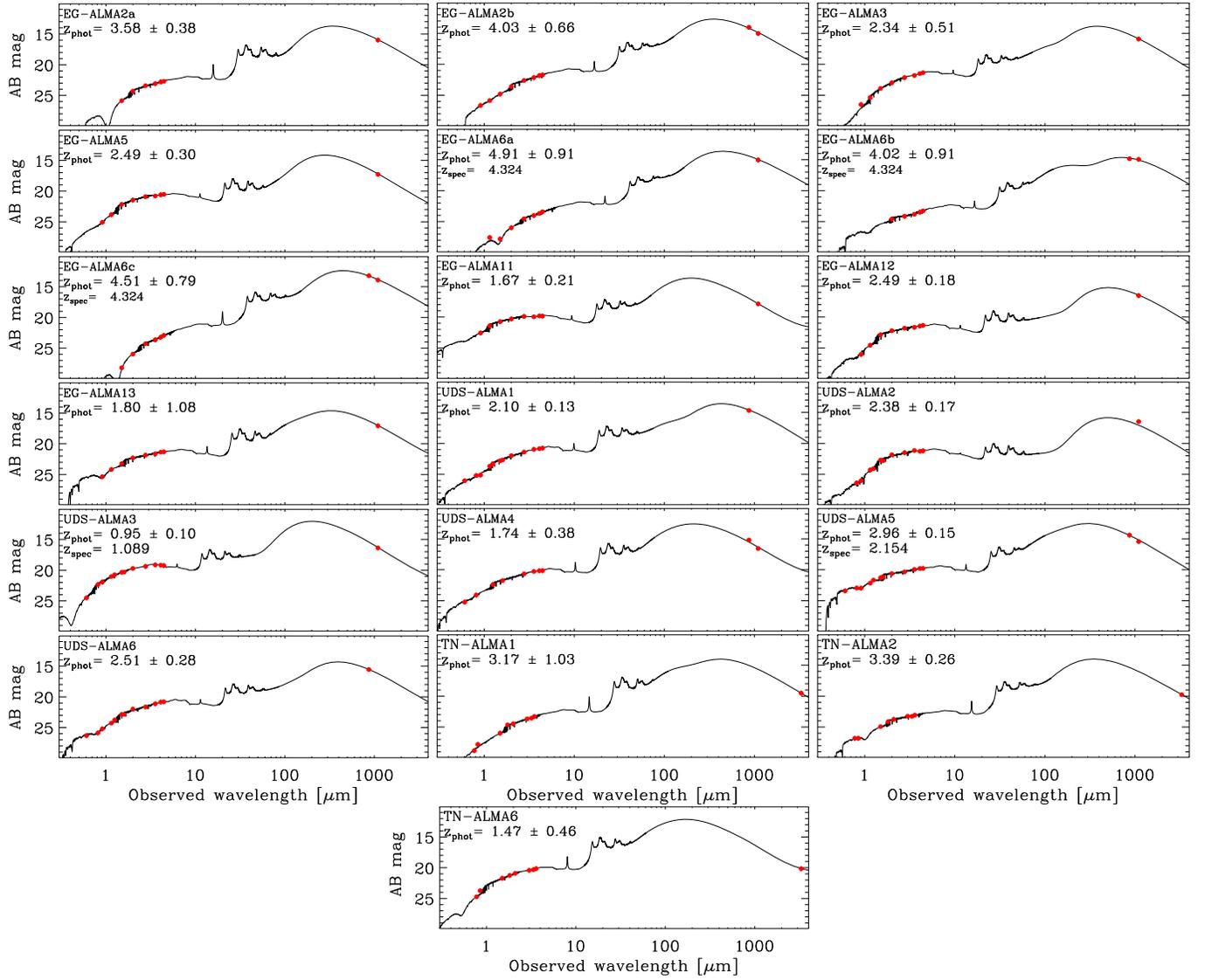
Figure 2. SED-fitting results using MAGPHYS-PHOTOZ. The legend in each panel gives the z_{spec} value when available. The red dots show the observed data, and the thick black lines show the best-fit templates. The multiply imaged systems EG-ALMA 2a/2b and EG-ALMA 6a/6b/6 c suffer from unreliable photometry because of the lensing distortion, and therefore the fits for individual images for the individual images have large error bars. UDS-ALMA 2 is a point source and very likely a quasar, and therefore the stellar templates used by MAGPHYS-PHOTOZ might not be applicable. It is still shown here for completeness. We note that the photometric redshifts and uncertainties agree well with the spectroscopic redshifts when these are available.

clearly seen in Figure 4 (middle). The mean ratio of specific SFR (sSFR) to main sequence is 0.24; the aforementioned three sources are below 0.10, which places them in the realm of quiescent galaxies. In other words, their host galaxies have already built up the bulk of their stellar masses, and their ongoing star formation, while detectable from the submillimeter/millimeter emission, is not significantly increasing the host's stellar mass. The usual *UVJ* diagnostic (Figure 4 right) shows that the three quiescent hosts are indeed in the conventional quiescent-galaxy region (Labbe et al. 2005; Williams et al. 2009), verifying the low sSFR.

3.3. Morphology of Host Galaxies

The NIRCam images (Figure 1) allow morphologies to be determined for 13 of the ALMA source hosts.[27] By our visual

classification, all 13 show nondisturbed (or weakly disturbed) disks even though some of them (e.g., UDS-ALMA 4) might have features indicative of a recent minor merger.[28]

To further study the morphologies, we ran GALFIT (Peng et al. 2002) to fit Sérsic profiles to the galaxies' F444W or F360M images (the latter only for the three TNJ1338 sources). The results are shown in Figure 5 and detailed in Appendix B. Briefly, the fitted Sérsic indices n are near 1 (median $\langle n \rangle = 1.1 \pm 0.8$), consistent with disky galaxies. The GALFIT run also computed half-light radii (R_e) based on the best-fit profile and excluding a central point source when one was present. At the source redshifts, F444W or F360M samples the rest-frame visible-to-near-IR range, and therefore this R_e reflects the stellar mass distribution. In other words, R_e is a proxy for the half-mass radius. The median R_e of our sample is

---

[27] The two multiply imaged systems in El Gordo are highly distorted, and UDS-ALMA 2 is a point source and potentially hosts a quasar. Morphologies cannot be determined for these.

[28] EG-ALMA 11 has a close neighbor comparable in size, but the neighbor's spectroscopic redshift $z_{spec} = 0.87$ shows that it is a foreground galaxy.
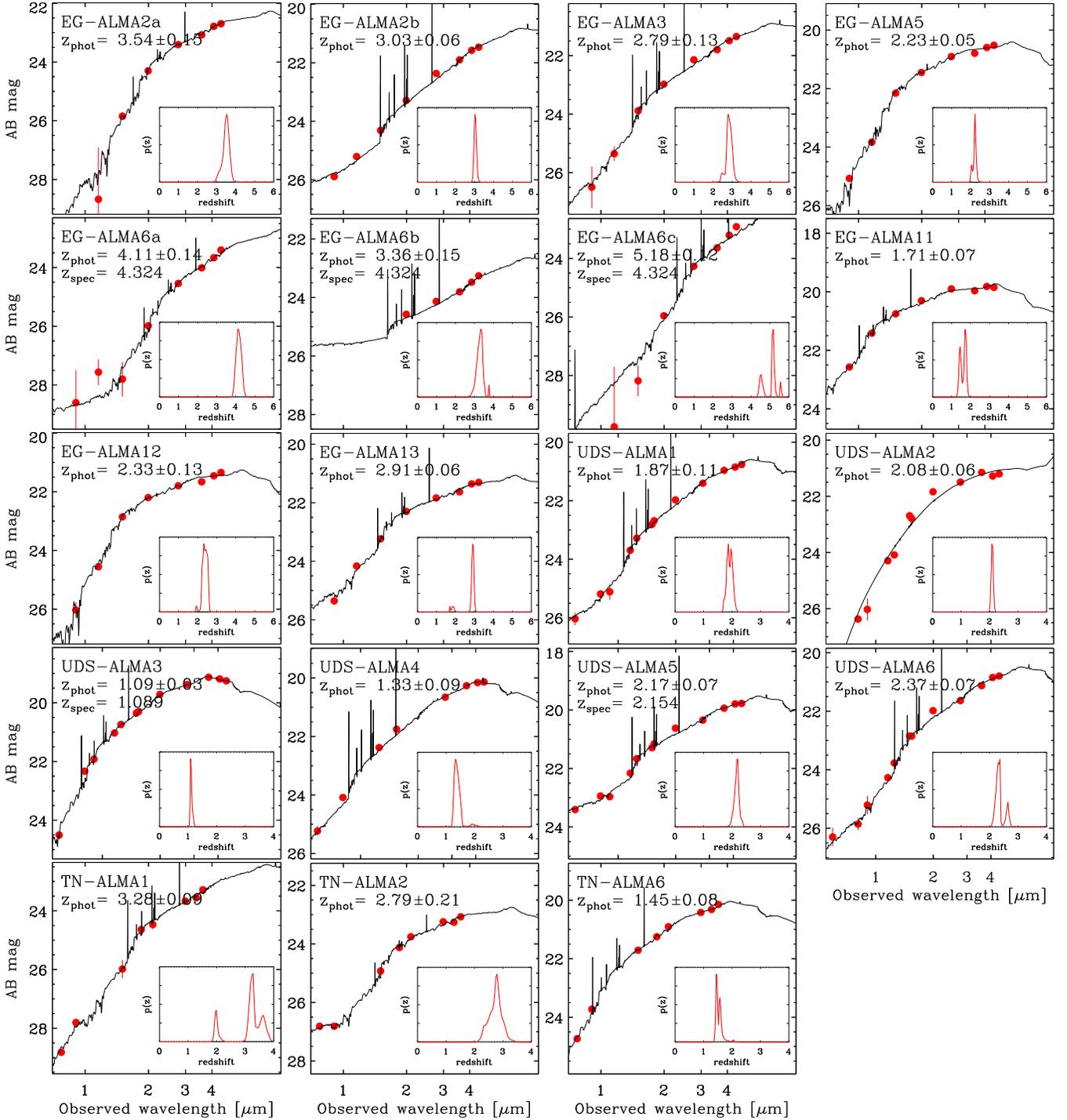
Figure 3. Results of EAZY fitting to derive z_{phot} independently. Points show observed data, and solid lines show the best-fit templates. Best-fit redshift is indicated in each panel. Insets show the redshift probability distributions. For UDS-ALMA 3, $z_{spec} = 1.089$ and for UDS-ALMA 5, $z_{spec} = 2.154$, which are both in excellent agreement with the photometric redshift estimates from EAZY listed in their figure panels. UDS-ALMA 2 is fitted using the AGN templates, and the best-fit template is the obscured AGN A2690#75 from Fiore et al. (2008). The vertical scales of all panels cover a 7 mag range, though with differing offsets, to allow comparison of the SEDs.

1.6 kpc with bootstrap uncertainty 0.4 kpc. The dispersion of the whole sample is 1.4 kpc. For comparison, the median R_e of the disk galaxies among the far-IR/SMG sample ($0.5 \lesssim z \lesssim 3$) of Ling & Yan (2022) is 3.6 kpc. Figure 6 shows the mass–size distributions of our ALMA sources as well as those of the few recently published NIRCam results in other fields. The mass–size relations of star-forming and quiescent galaxies from Suess et al. (2019, their Figure 7) are also shown for comparison. Qualitatively, most of our sources fall below the relation for star-forming galaxies and are more in line with that of quiescent galaxies, despite the fact that most of our sources are not quiescent. In contrast, the ultrared, flattened, disky galaxies recently found by Nelson et al. (2022) have larger R_e and follow more closely the relation for star-forming galaxies. A larger sample will be needed to further investigate this problem.
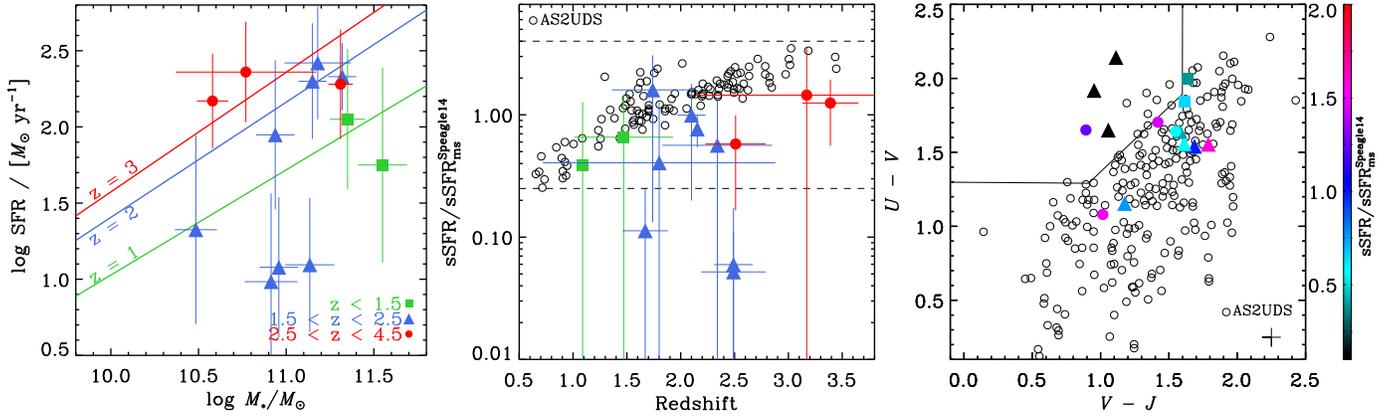
Figure 4. Stellar population properties of the JWST counterparts of the ALMA sources. The two multiply imaged systems EG-ALMA 2a/2b, EG- ALMA 6a/6b/6 c and the point source UDS-ALMA 2 are excluded. Left: star formation rate versus stellar mass. All values have been corrected for magnification. The points with error bars represent the 13 galaxies, and the lines show the star formation main sequence (Speagle et al. 2014). The points and lines are color coded by redshift as labeled and indicated in the legend. Middle: ratios of the specific star formation rates of our sources to those of the main sequence galaxies as a function of redshift. The colored points with error bars are the 13 ALMA sources, and the open circles show the SMGs from the AS2UDS program (Dudzevičiūtė et al. 2020) for comparison. The dashed horizontal lines (ratios of 1/4 and 4, respectively) indicate the nominal range within which galaxies are considered to be on the main sequence. Right: *UVJ* color–color diagram. The points represent the ALMA-source host galaxies, color coded by their sSFR/sSFR$_{ms}$ values as indicated by the color bar to the right. The rest-frame *UVJ* colors were computed by EAZY from the best-fit templates at the adopted redshifts. The cross in the lower right corner indicates our estimate of the typical uncertainties. The black open circles show the *UVJ* colors of the AS2UDS SMGs (Stach et al. 2019) for comparison. The quiescent-galaxy region marked by solid lines in the upper left is based on Patel et al. (2012). The one blue data point in this region is TN-ALMA 2 ($z_{phot} = 2.79$). Its reddest passband, F360M, does not reach the rest-frame *J* band, and therefore EAZY's estimate of its $V - J$ color has large uncertainty.

4. Discussion

4.1. Sample Selection Effect

By virtue of their submillimeter/millimeter emission, the ALMA sources discussed in this work are SMGs. However, they include many sources fainter than the bulk of the SMG population previously studied in the literature. This is because of the combination of the gravitational lensing by a cluster in one of our survey fields and that most of our sources were not preselected by surveys using single-dish submillimeter/millimeter telescopes but were serendipitous discoveries in ALMA maps of various depths. The ALMA maps are deeper than any single-dish survey, and therefore most of our ALMA sources are fainter than those from the usual SMG samples. This is demonstrated in Figure 7. Specific to the El Gordo field, the median $S_{870\mu m}$ flux density of our sample is 1.1 mJy after correcting for the lensing magnification. If we exclude the two multiply imaged systems, the median $S_{870\mu m}$ drops to 0.5 mJy in the El Gordo field, and the median $S_{870\mu m}$ of the whole sample is 2 mJy. In contrast, the AS2UDS sample has median $S_{870\mu m} = 3.6$ mJy and reaches down to 0.6 mJy. Our sample therefore includes more SMGs with low-to-moderate SFRs, which explains why most of our sources exhibit properties (e.g., their nondisturbed disky morphologies) different from those often described in the literature. On the other hand, it is not surprising that most $z \gtrsim 2$ galaxies should have some low-level, ongoing star formation. Due to the high sensitivity of ALMA, our sample is more sensitive than the single-dish-preselected SMG samples in probing such activity.

4.2. Disk Galaxy Evolution

After excluding the two multiply imaged systems (EG-ALMA 2a/2b and EG-ALMA 6a/6b/6c) and the quasar (UDS-ALMA 2), the remaining 13 ALMA source hosts in our sample are all disk galaxies, mostly showing little sign of disturbance suggestive of major mergers. The two ALMA sources of Cheng et al. (2022) that are large enough for

morphological study are similar systems. This would be a surprising result in the pre-JWST era. However, recent JWST/NIRCam morphological studies of the general galaxy population have shown that disk galaxies are already common at $z > 1.5$ (Ferreira et al. 2022a, 2022b; Jacobs et al. 2022). If star formation at $z \approx 1–3$ mostly happens in disk galaxies, it can explain why our ALMA source hosts are mostly such systems.

All these 13 disk galaxies have already acquired large stellar masses, which range from 0.3 to $3.5 \times 10^{11} M_\odot$. As they have no indication of being major mergers, these galaxies most likely assembled the majority of their stars through secular growth (e.g., Guo et al. 2022), although we cannot rule out the role of minor mergers. Given their SFRs of 10–300 $M_\odot$ yr^{-1}, their sSFRs spread them over both the star-forming main sequence and the quiescent categories. Three of them are deemed quiescent galaxies based on their sSFRs. These same three galaxies are also in the quiescent region in the rest-frame *UVJ* diagram, which is to say that their UV-to-near-IR emissions show no sign of ongoing star formation. Had there not been ALMA revealing their low-level star formation hidden by dust (SFRs of 10–15 $M_\odot$ yr^{-1}), they would be viewed as "red-and-dead" and yet disky galaxies. These galaxies are similar to those recently reported by Nelson et al. (2022) in the sense that they are also red disky galaxies; the difference is that ours are still detected in the HST bands. Future morphological study within the same ALMA coverage will reveal whether there really are disk galaxies that have completely ceased star formation.

Another interesting result is that our galaxies have a wide range of half-light (equivalently, half-mass) radii R_e. EG-ALMA 3 has the largest $R_e = 5.35 \pm 0.27$ kpc, while EG-ALMA 13 has the smallest $R_e = 1.08 \pm 0.21$ kpc. EG-ALMA 3 ($z_{phot} = 2.34$, $M_* = 8.7 \times 10^{10} M_\odot$, SFR = 87 $M_\odot$ yr^{-1}) is similar to the recently reported grand-design spiral galaxy A2744-DSG-z3 at $z = 3.06$ (Wu et al. 2022), which has $R_e = 7.3 \pm 0.8$ kpc and $M_* = 4.0 \times 10^{10} M_\odot$. The latter is also an ALMA source and has SFR = 85 $M_\odot$ yr^{-1} based on its
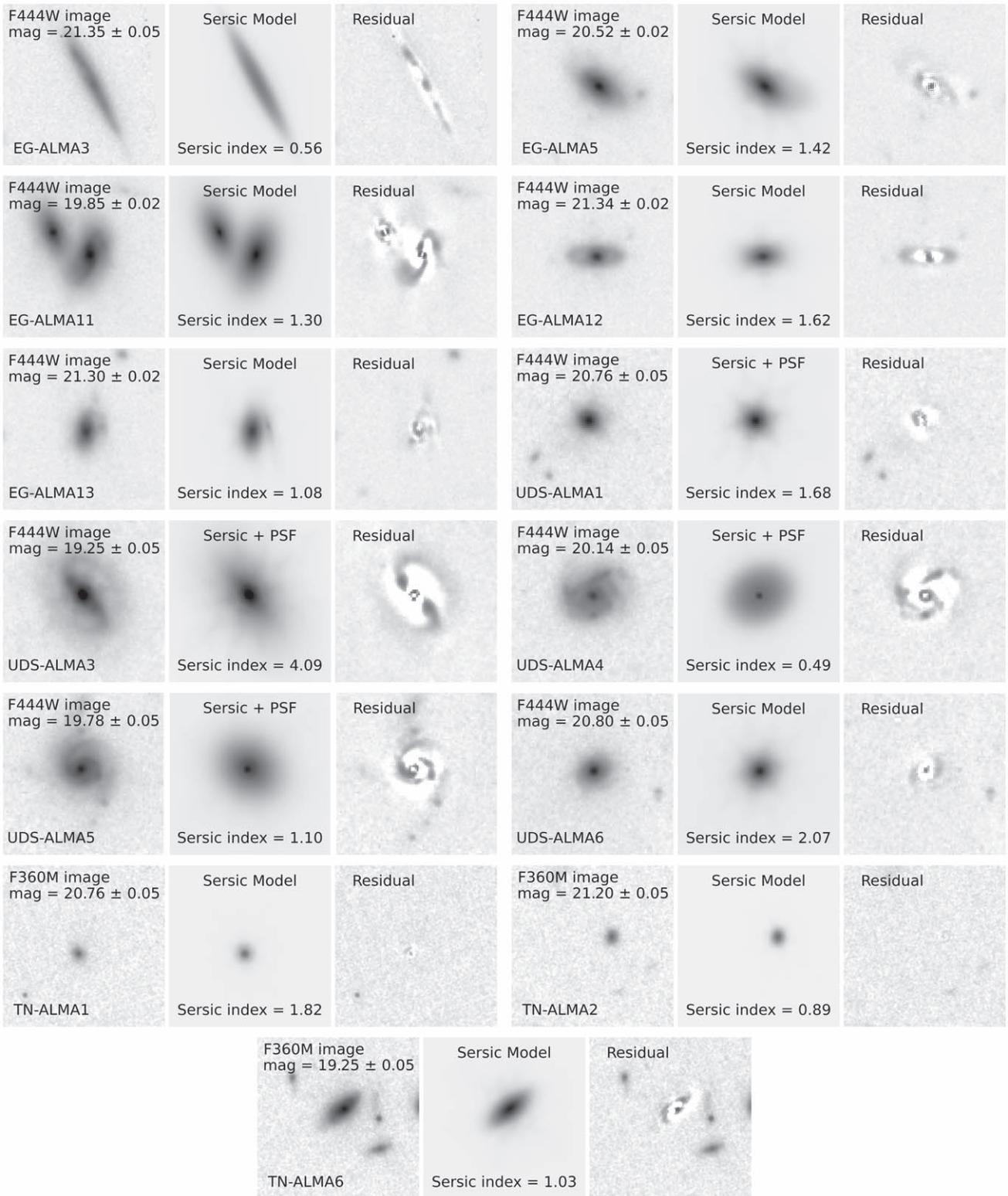
Figure 5. GALFIT fitting results of our sources. The two multiply imaged systems (EG-ALMA 2a/2b and EG-ALMA 6a/6b/6c) and the quasar (UDS-ALMA 2) are not included. From left to right, three panels show the original F444W (or F360M) negative image (with source name and filter noted), the fitted Sérsic model (with the index noted), and the residual (the original image with model subtracted), respectively. The images are centered on the ALMA positions and are 5″ (∼40 kpc) on a side. The depth of the TNJ1338 images is shallower than the rest, so we stacked the F300M, F335M, and F360M images to synthesize deeper broadband images with 3× longer exposure. Fitting models to the stacked images (not shown) gave sizes consistent with those from the F360M images.

far-IR-to-millimeter luminosity (Sun et al. 2022). Such large disks are rare in our sample; however, the median R_e of our sample is 1.6 kpc, which means that our targets are predominantly small disks. The sizes of the general disk-galaxy population at $z > 1.5$ is still awaiting investigation, and therefore it is unclear whether our sample being dominated by small disks
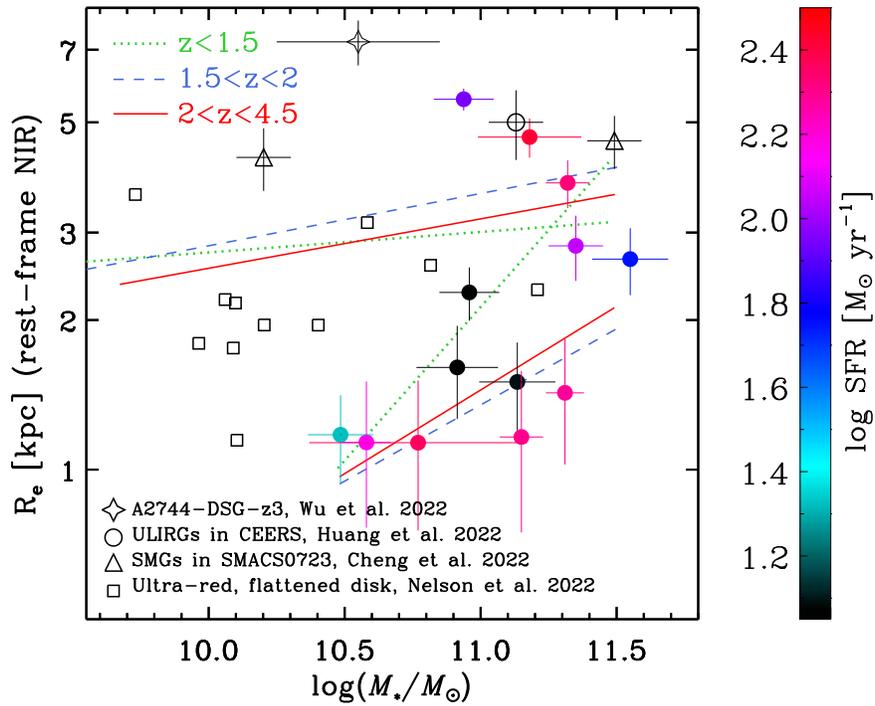
Figure 6. Stellar half-light radii versus stellar mass for ALMA source hosts in Figure 5. The filled symbols represent our objects, which are color coded based on their SFRs. The color bar on the right shows the coding. For comparison, the open symbols show the ultrared, flattened disks (Nelson et al. 2022), SMGs in SMACS 0723 (Cheng et al. 2022), ULIRGs in CEERS (J.-S. Huang et al. 2022 in preparation), and the SMG in A2744 (Wu et al. 2022), respectively. All values are based on NIRCam data, and we remeasured the sources in SMACS 0723 using GALFIT for consistency. The color-coded straight lines, based on the CANDELS results (Suess et al. 2019), show the relations for quiescent (lower group) and star-forming (upper group) galaxies in three redshift ranges as indicated. Most of our sources, despite the fact that they are forming stars at high rates, have sizes in the range for quiescent galaxies.

is normal or is caused by some selection bias that is still unknown to us.

5. Summary

While our sample consists of only 16 unique objects, it is the largest to date that has both ALMA and JWST/NIRCam data. The ALMA positions enabled us to pinpoint unambiguous NIRCam counterparts. Due to the high sensitivities of the ALMA data, our sample is more inclusive than the classic SMG samples in that our sources show a much wider range of properties. We are able to probe dust-embedded star formation as low as $\sim 10 \; M_\odot \, \mathrm{yr}^{-1}$. The deep, high-resolution NIRCam data detect the rest-frame near-IR emission from long-lived stars that dominate the stellar masses, and most of our sources are high-mass ($M_* > 10^{10.5} \; M_\odot$) galaxies with typically nondisturbed disks. Furthermore, most of them have small-to-medium half-mass radii (median of only 1.6 kpc), suggesting that they are small disks. We postulate that secular growth can be a viable route to build high-mass disk galaxies and that we can now see snapshots of such processes in the submillimeter/millimeter regime in a similar way as in UV-to-IR wavelengths. Of course, we will need a much larger sample to have sufficient statistics in different mass, morphology, and redshift bins. This calls for the synergy of ALMA and JWST.
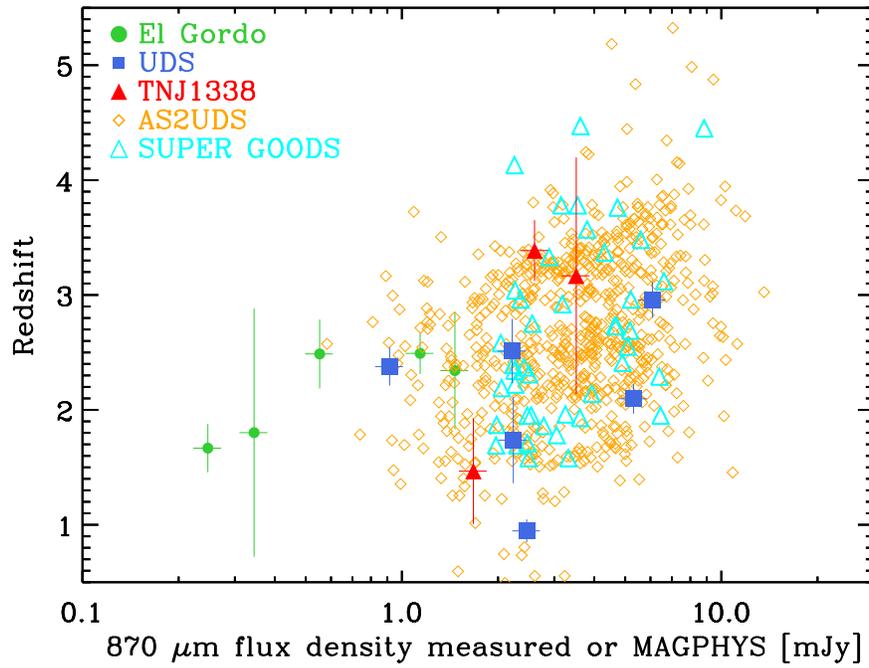
Figure 7. SMG redshifts vs. 870 μm flux density. Green circles represent sources in El Gordo (with delensed flux densities), blue squares sources in UDS, and red triangles TNJ1338. For sources that do not have direct S_{870} measurements (see Table 1), synthesized flux densities based on the best-fit templates from MAGPHYS are shown. Open orange diamonds show the AS2UDS sample (Stach et al. 2019), and open cyan triangles show the SUPER GOODS (Cowie et al. 2018) sample. The two multiply lensed systems, EG-ALMA 2a/2b and EG-ALMA 6a/6b/6 c, are excluded, leaving 14 targets.

This paper makes use of the following ALMA data: ADS/ JAO.ALMA#2013.1.01358.S, 2018.1.00035.L, 2013.1.01051.S, 2015.1.00530.S, 2012.1.00326.S, 2016.1.01184.S, 2013.1.00356. S, 2015.1.01105.S, 2013.1.00781.S, 2015.1.00442.S, 2015.1. 01074.S,2015.1.01528.S, 2017.1.01027.S. ALMA is a partnership of ESO (representing its member states), NSF (USA) and NINS (Japan), together with NRC (Canada), MOST and ASIAA (Taiwan), and KASI (Republic of Korea), in cooperation with the Republic of Chile. The Joint ALMA Observatory is operated by ESO, AUI/NRAO and NAOJ. The National Radio Astronomy Observatory is a facility of the National Science Foundation operated under cooperative agreement by Associated Universities, Inc. The ALMA data reduction and other data services of this work are fully or partially supported by China-Chile Astronomical Data Center (CCADC), which is affiliated to Chinese Academy of Sciences South America Center for Astronomy (CASSACA).

Facilities: HST, JWST, MAST (https://archive.stsci.edu), ALMA.

Software: astropy (Astropy Collaboration et al. 2013, 2018), Source Extractor (Bertin & Arnouts 1996), GALFIT (Peng et al. 2002), EAZY (Brammer et al. 2008), CASA (McMullin et al. 2007), MAGPHYS (da Cunha et al. 2008).

Appendix A
Z_{phot} with Different Methods

Figure A1 compares the z_{phot} fitting results with EAZY and MAGPHYS+PHOTOZ (Battisti et al. 2019), which take the ALMA flux into account. The results are consistent, implying that the main results of this work would not change if we used z_{phot}, stellar mass, and SFR from MAGPHYS+PHOTOZ instead of taking z_{phot} from EAZY.
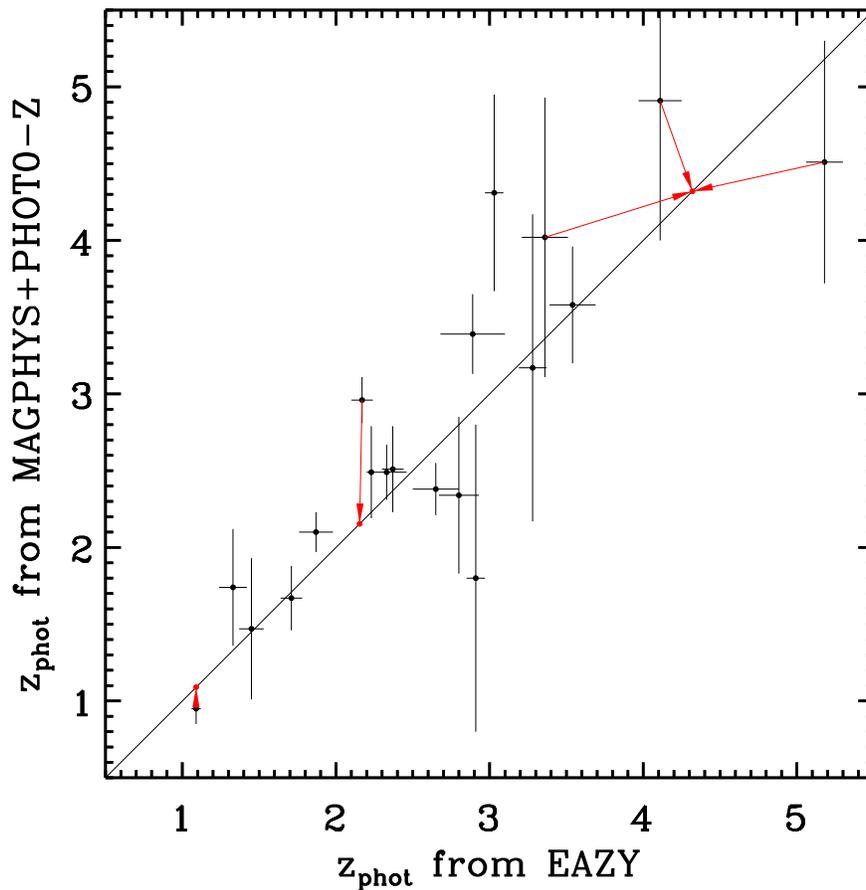
Figure A1. Comparison between z_{phot} from EAZY and MAGPHYS+PHOTOZ. Diagonal line shows equality for the two forms of z_{phot}. For three targets (UDS-ALMA 3, UDS-ALMA 5, EG-ALMA 6a/6b/6c) with known z_{spec}, red arrows connect the z_{phot} to the measured z_{spec}, indicated by red points.

Appendix B
Sérsic Profile Fitting

Figure 5 shows the fitted GALFIT models, which are based on a Sérsic function plus a central point source. Figure B1 shows the distribution of the derived Sérsic indices with size. The

NIRCam images of TNJ1338 were obtained through medium-band filters and are shallower. To check whether this biases the fitting, we combined all three long-wavelength medium-band images and ran GALFIT again on this composite image. The R_e values thus derived agree with the ones based on the F360M image.
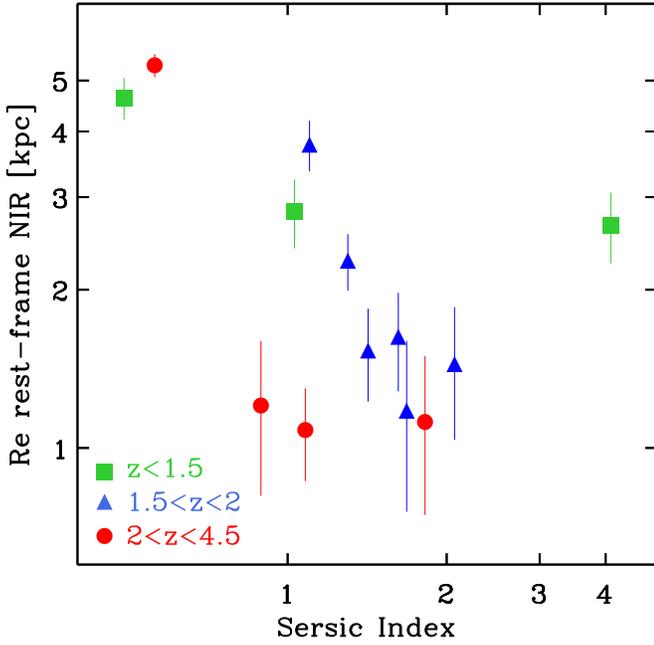
Figure B1. Half-light radii vs. Sérsic indices for our SMG sample. UDS-ALMA 1/3/4/5 have compact cores, which were subtracted when calculating the half-light radii, as here we are interested only in their disk components. The SMG with $n \sim 4$ is UDS-ALMA 3, which has a point source, a bar, and spiral components that skew the model fit.

Appendix C
EG-ALMA 6 c: An F160W-faint SMG

Previous studies have revealed a population of dusty near-IR-faint galaxies (Frayer et al. 2004; Huang et al. 2011; Wang et al. 2019; Sun et al. 2021; Smail et al. 2021) that are very faint or even invisible in HST/WFC3 F160W (the reddest HST band). This has led to the name "HST dark," but they are prominent sources in Spitzer/IRAC 3.6 and 4.5 μm images. These could be either passive or dusty galaxies at $z \geqslant 3$. Our sample contains one such source, the triply imaged system EG-ALMA 6a/6b/6 c. EG-ALMA 6 c is the most highly magnified of the three images. It is adjacent to the source "ID #4a"[29] of Caputi et al. (2021), which is part of their galaxy group at $z \simeq 4.32$. The MUSE spectrum of ID #4a yields $z = 4.3196$ based on absorption lines such as Lyα, Si II, and C II. From our NIRCam images, ID #4a and EG-ALMA 6 c are separated by $1\rlap{.}''4$, which corresponds to 9 kpc at $z = 4.32$. The host of this ALMA source is much redder than ID #4a. Fortunately, there are archival ALMA Band-3 spectral scans in this region, which we reduced following the standard process. There is a strong, double-peaked emission line at 86.6 GHz (Figure C1). If EG-ALMA 6 c is at a similar redshift to ID #4a, this line is CO $J = 4$–3, and the redshift corresponds to $z = 4.324$, showing that ID #4a and EG-ALMA 6 c are distinct sources. The two peaks of the 86.6 GHz line are separated by 380 km s^{-1}, which suggests that the source is likely massive but similar to other submillimeter galaxies (Birkin et al. 2021). The integrated CO (4–3) flux is 0.79 ± 0.08 mJy km s^{-1}, which corresponds to $M_{H_2} = 10^{9.8 \pm 1.0}$ $M_{\odot}$ (magnification-factor-corrected), adopting $L'_{CO\,(4-3)}/L'_{CO\,(1-0)} = 0.46$, $\alpha_{CO} = 0.8$ $M_{\odot}$ (K km s^{-1} pc^2)$^{-1}$ for SMGs (Carilli & Walter 2013). The depletion timescale

---

[29] In the naming scheme of Caputi et al. (2021), ID #4 refers to the lensed source, and suffixes a, b, and c refer to the three lensed images.
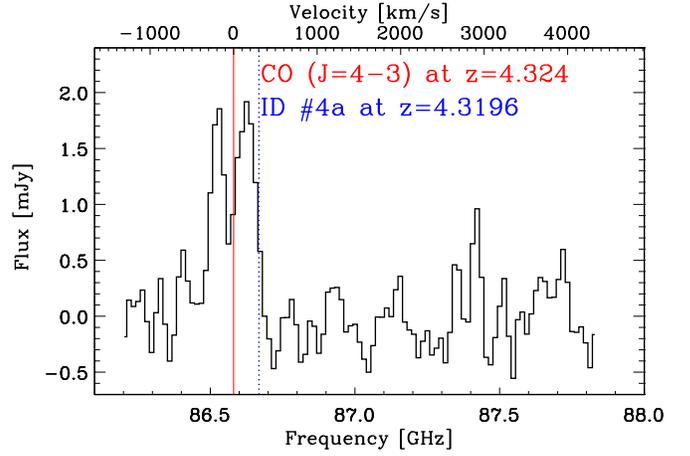

Figure C1. Spectrum of EG-ALMA 6 c from the ALMA 92 GHz data cube. The solid red line shows the flux-weighted central frequency of the observed emission line. If this line is CO $J = 4$–3, its redshift is 4.324. This is consistent with the lensing model of Caputi et al. (2021). The dashed blue line shows where the CO $J = 4$–3 line would be centered at the redshift of source ID #4a (Caputi et al. 2021).
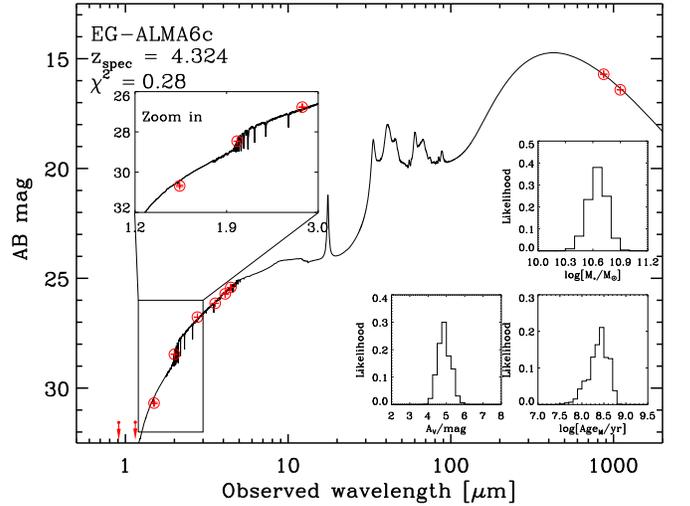

Figure C2. MAGPHYS fitting results for EG-ALMA 6 c. Red circles show the NIRCam photometry (using a $0\rlap{.}''6$ circular aperture) and the ALMA photometry. The two red arrows indicate the 3σ upper limits in the F090W and F115W bands. All values are demagnified. The black curve is the best-fitting model at the spectroscopic redshift $z = 4.324$. The three insets on the right are the probability density functions of the stellar mass M_*, extinction A_V, and mass-weighted age. The inset on the left shows the SED near the Balmer break.

M_{H_2}/SFR is about 70 Myr, which is close to the typical depletion timescales for local ULIRGs.

The velocity difference between EG-ALMA 6 c and ID #4a is ~250 km s^{-1}, suggesting that the two might be interacting. As ID #4a is not seen in the ALMA map, it must have very little cold dust. Its low gas content is consistent with the absence of emission lines in the ID #4a MUSE spectrum.

Figure C2 shows the MAGPHYS SED-fitting results (demagnified) for EG-ALMA 6 c at $z = 4.324$. We highlight the F150W, F200W, and F277W SED to show that F150W-faint targets could be dusty galaxies at $z \sim 4$.

ORCID iDs

Cheng Cheng https://orcid.org/0000-0003-0202-0534
Jia-Sheng Huang https://orcid.org/0000-0001-6511-8745

Ian Smail ⬤ https://orcid.org/0000-0003-3037-257X
Haojing Yan ⬤ https://orcid.org/0000-0001-7592-7714
Seth H. Cohen ⬤ https://orcid.org/0000-0003-3329-1337
Rolf A. Jansen ⬤ https://orcid.org/0000-0003-1268-5230
Rogier A. Windhorst ⬤ https://orcid.org/0000-0001-8156-6281
Zhiyuan Ma ⬤ https://orcid.org/0000-0003-3270-6844
Anton Koekemoer ⬤ https://orcid.org/0000-0002-6610-2048
Christopher N. A. Willmer ⬤ https://orcid.org/0000-0001-9262-9997
S. P. Willner ⬤ https://orcid.org/0000-0002-9895-5758
Jose M. Diego ⬤ https://orcid.org/0000-0001-9065-3926
Brenda Frye ⬤ https://orcid.org/0000-0003-1625-8009
Christopher J. Conselice ⬤ https://orcid.org/0000-0003-1949-7638
Leonardo Ferreira ⬤ https://orcid.org/0000-0002-8919-079X
Andreea Petric ⬤ https://orcid.org/0000-0003-4030-3455
Min Yun ⬤ https://orcid.org/0000-0001-7095-7543
Hansung B. Gim ⬤ https://orcid.org/0000-0003-1436-7658
Maria del Carmen Polletta ⬤ https://orcid.org/0000-0001-7411-5386
Kenneth J. Duncan ⬤ https://orcid.org/0000-0001-6889-8388
Benne W. Holwerda ⬤ https://orcid.org/0000-0002-4884-6756
Huub J. A. Röttgering ⬤ https://orcid.org/0000-0001-8887-2257
Rachel Honor ⬤ https://orcid.org/0000-0002-9984-4937
Nimish P. Hathi ⬤ https://orcid.org/0000-0001-6145-5090
Patrick S. Kamieneski ⬤ https://orcid.org/0000-0001-9394-6732
Nathan J. Adams ⬤ https://orcid.org/0000-0003-4875-6272
Dan Coe ⬤ https://orcid.org/0000-0001-7410-7669
Tom Broadhurst ⬤ https://orcid.org/0000-0002-5807-4411
Jake Summers ⬤ https://orcid.org/0000-0002-7265-7920
Scott Tompkins ⬤ https://orcid.org/0000-0001-9052-9837
Simon P. Driver ⬤ https://orcid.org/0000-0001-9491-7327
Norman A. Grogin ⬤ https://orcid.org/0000-0001-9440-8872
Madeline A. Marshall ⬤ https://orcid.org/0000-0001-6434-7845
Nor Pirzkal ⬤ https://orcid.org/0000-0003-3382-5941
Aaron Robotham ⬤ https://orcid.org/0000-0003-0429-3579
Russell E. Ryan, Jr. ⬤ https://orcid.org/0000-0003-0894-1588

References

Astropy Collaboration, Price-Whelan, A. M., Sipőcz, B. M., et al. 2018, AJ, 156, 123
Astropy Collaboration, Robitaille, T. P., Tollerud, E. J., et al. 2013, A&A, 558, A33
Battisti, A. J., da Cunha, E., Grasha, K., et al. 2019, ApJ, 882, 61
Bertin, E., & Arnouts, S. 1996, A&AS, 117, 393
Birkin, J. E., Weiss, A., Wardlow, J. L., et al. 2021, MNRAS, 501, 3926
Blain, A. W. 1996, MNRAS, 283, 1340
Blain, A. W., Smail, I., Ivison, R. J., Kneib, J. P., & Frayer, D. T. 2002, PhR, 369, 111
Bourne, N., Dunlop, J. S., Simpson, J. M., et al. 2019, MNRAS, 482, 3135
Brammer, G. B., van Dokkum, P. G., & Coppi, P. 2008, ApJ, 686, 1503
Caputi, K. I., Caminha, G. B., Fujimoto, S., et al. 2021, ApJ, 908, 146
Cardona-Torres, L., Aretxaga, I., Montaña, A., Zavala, J. A., & Faber, S. M. 2022, MNRAS, Advance Access

Carilli, C. L., & Walter, F. 2013, ARA&A, 51, 105
Casey, C. M., Narayanan, D., & Cooray, A. 2014, PhR, 541, 45
Chen, C.-C., Gao, Z.-K., Hsu, Q.-N., et al. 2022, ApJL, 939, L7
Chen, C.-C., Smail, I., Swinbank, A. M., et al. 2015, ApJ, 799, 194
Cheng, C., Ibar, E., Smail, I., et al. 2020, MNRAS, 499, 5241
Cheng, C., Yan, H., Huang, J.-S., et al. 2022, ApJL, 936, L19
Coe, D., Salmon, B., Bradač, M., et al. 2019, ApJ, 884, 85
Cowie, L. L., Gonzalez-Lopez, J., Barger, A. J., et al. 2018, ApJ, 865, 106
da Cunha, E., Charlot, S., & Elbaz, D. 2008, MNRAS, 388, 1595
De Breuck, C., van Breugel, W., Minniti, D., et al. 1999, A&A, 352, L51
Diego, J. M., Meena, A. K., Adams, N. J., et al. 2022, arXiv:2210.06514
Diego, J. M., Molnar, S. M., Cerny, C., et al. 2020, ApJ, 904, 106
Dudzevičiūtė, U., Smail, I., Swinbank, A. M., et al. 2020, MNRAS, 494, 3828
Duncan, K. J., Windhorst, R. A., Koekemoer, A. M., et al. 2022, arXiv:2212.09769
Dunlop, J. S., Abraham, R. G., Ashby, M. L. N., et al. 2021, PRIMER: Public Release IMaging for Extragalactic Research, JWST Proposal. Cycle 1, ID #1837
Dunlop, J. S., McLure, R. J., Biggs, A. D., et al. 2017, MNRAS, 466, 861
Ferreira, L., Adams, N., Conselice, C. J., et al. 2022a, ApJL, 938, L2
Ferreira, L., Conselice, C. J., Sazonova, E., et al. 2022b, arXiv:2210.01110
Fiore, F., Grazian, A., Santini, P., et al. 2008, ApJ, 672, 94
Fomalont, E., van Kempen, T., Kneissl, R., et al. 2014, Msngr, 155, 19
Frayer, D. T., Reddy, N. A., Armus, L., et al. 2004, AJ, 127, 728
Grogin, N. A., Kocevski, D. D., Faber, S. M., et al. 2011, ApJS, 197, 35
Guo, Y., Jogee, S., Finkelstein, S. L., et al. 2022, arXiv:2210.08658
Hodge, J. A., Karim, A., Smail, I., et al. 2013, ApJ, 768, 91
Hodge, J. A., Smail, I., Walter, F., et al. 2019, ApJ, 876, 130
Hodge, J. A., Swinbank, A. M., Simpson, J. M., et al. 2016, ApJ, 833, 103
Huang, J.-S., Zheng, X. Z., Rigopoulou, D., et al. 2011, ApJL, 742, L13
Jacobs, C., Glazebrook, K., Calabrò, A., et al. 2022, arXiv:2208.06516
Jee, M. J., Hughes, J. P., Menanteau, F., et al. 2014, ApJ, 785, 20
Koekemoer, A. M., Faber, S. M., Ferguson, H. C., et al. 2011, ApJS, 197, 36
Labbe, I., Huang, J., Franx, M., et al. 2005, ApJL, 624, L81
Lang, P., Schinnerer, E., Smail, I., et al. 2019, ApJ, 879, 54
Lindner, R. R., Baker, A. J., Hughes, J. P., et al. 2014, ApJ, 786, 49
Ling, C., & Yan, H. 2022, ApJ, 929, 40
Marriage, T. A., Acquaviva, V., Ade, P. A. R., et al. 2011, ApJ, 737, 61
McMullin, J. P., Waters, B., Schiebel, D., Young, W., & Golap, K. 2007, in ASP Conf. Ser. 376, Astronomical Data Analysis Software and Systems XVI, ed. R. A. Shaw, F. Hill, & D. J. Bell (San Francisco, CA: ASP), 127
Menanteau, F., Gonzalez, J., Juin, J.-B., et al. 2010, ApJ, 723, 1523
Menanteau, F., Hughes, J. P., Sifon, C., et al. 2012, ApJ, 748, 7
Miley, G. K., Overzier, R. A., Tsvetanov, Z. I., et al. 2004, Natur, 427, 47
Negrello, M., Amber, S., Amvrosiadis, A., et al. 2017, MNRAS, 465, 3558
Negrello, M., Hopwood, R., De Zotti, G., et al. 2010, Sci, 330, 800
Nelson, E. J., Suess, K. A., Bezanson, R., et al. 2022, arXiv:2208.01630
Patel, S. G., Holden, B. P., Kelson, D. D., et al. 2012, ApJL, 748, L27
Peng, C. Y., Ho, L. C., Impey, C. D., & Rix, H.-W. 2002, AJ, 124, 266
Perrotta, F., Baccigalupi, C., Bartelmann, M., de Zotti, G., & Granato, G. L. 2002, MNRAS, 329, 445
Smail, I., Dudzeviciute, U., Stach, S. M., et al. 2021, MNRAS, 502, 3426
Smail, I., Ivison, R. J., & Blain, A. W. 1997, ApJL, 490, L5
Speagle, J. S., Steinhardt, C. L., Capak, P. L., & Silverman, J. D. 2014, ApJS, 214, 15
Stach, S. M., Dudzeviciute, U., Smail, I., et al. 2019, MNRAS, 487, 4648
Stach, S. M., Smail, I., Swinbank, A. M., et al. 2018, ApJ, 860, 161
Suess, K. A., Kriek, M., Price, S. H., & Barro, G. 2019, ApJL, 877, 103
Sun, F., Egami, E., Fujimoto, S., et al. 2022, ApJ, 932, 77
Sun, F., Egami, E., Perez-Gonzalez, P. G., et al. 2021, ApJ, 922, 114
Venemans, B. P., Kurk, J. D., Miley, G. K., et al. 2002, ApJL, 569, L11
Wang, T., Schreiber, C., Elbaz, D., et al. 2019, Natur, 572, 211
Williams, R. J., Quadri, R. F., Franx, M., van Dokkum, P., & Labbe, I. 2009, ApJ, 691, 1879
Windhorst, R. A., Cohen, S. H., Jansen, R. A., et al. 2023, AJ, 165, 13
Wu, Y., Cai, Z., Sun, F., et al. 2022, arXiv:2208.08473
Yan, H., Cohen, S. H., Windhorst, R. A., et al. 2022, arXiv:2209.04092
Zavala, J. A., Buat, V., Casey, C. M., et al. 2022, arXiv:2208.01816
Zitrin, A., Menanteau, F., Hughes, J. P., et al. 2013, ApJL, 770, L15